eprints@whiterose.ac.uk
https://eprints.whiterose.ac.uk/

Full length article

Novel plasma treatment for preparation of laser sintered nanocomposite parts

Alaa Almansoori[a,b,*], Kerry J. Abrams[a], Ammar D. Ghali Al-Rubaye[c,d], Candice Majewski[c], Cornelia Rodenburg[a]

[a] Department of Material Science and Engineering, University of Sheffield, UK
[b] Southern Technical University, Basra, Iraq
[c] Department of Mechanical Engineering, University of Sheffield, UK
[d] College of Engineering, University of Wasit, Wasit, Iraq

ABSTRACT

Polymer Laser Sintering (LS) is a well-known Additive Manufacturing process, capable of producing highly complex geometries with little or no cost penalty. However, the restricted range of materials currently available for this process has limited its applications. Whilst it is common to modify the properties of standard LS polymers with the inclusion of fillers e.g. nanoclays, achieving effective dispersions can be difficult. The work presented here investigates the use of plasma treatment as a method of enhancing dispersion with an expectation of improving consistency and surface quality of laser sintered nanocomposite parts. To enable the preparation of polyamide 12 nanocomposite powder for applications in LS, plasma surface modification using Low Pressure Air Plasma Treatment was carried out on two nanoclays: Cloisite 30B (C30B) and Nanomer I.34TCN (I.34TCN). Plasma treatment strongly reduced the aggregation of the nanoclay (C30B and I.34TCN) particles, and powders displayed higher decomposition temperatures than those without plasma treatment. LS parts from neat polyamide 12, untreated I.34TCN and plasma treated I.34TCN composites were successfully produced with different complex shapes. The presence of well dispersed plasma treated nanoclays was observed and found to be essential for an improved surface quality of LS fabricated which was achieved only for plasma treated I.34TCN. Likewise, some mechanical properties could be improved above that of PA12 by incorporation of treated I.34TCN. For example, the elastic modulus of plasma treated composites was higher than that of polyamide 12 and the untreated composite. In the case of the ultimate strain, the plasma treated composite performed better than untreated and results had a reduced variation between samples. This illustrates the feasibility of the use of plasma treatments on nanoclays to improve the properties of LS parts, even though further studies will be required to exploit the full potential.

1. Introduction

This study explores the effect of the plasma treatment process on the physico-chemical properties of two organo-modified nanoclay surfaces (Cloisite 30B (C30) and Nanomer I.34 TCN (I.34TCN) and the consequences for their applications in laser sintering (LS) polymer nanocomposites. LS is designed to build 3-dimensional (3D) products with complex and accurate geometries from powdered materials without the need for moulds or patterns [1–3]. Firstly, polymeric powder is preheated to a temperature below its melting point for a certain time. Then, a CO_2-laser selectively fuses the heated powder to produce products layer by layer. LS parameters such as laser power, scan speed,

scan spacing and layer thickness can be varied for optimised properties [4]. However, a limited selection of materials and inconsistent mechanical properties are still challenges, restricting the overall potential of LS [5–8]. Porosity and surface quality also affect the functions of the end-use parts [9,10]. Pore formation is highly affected by the melt flow and thermal stability and is also influenced by the powder particle shape, distribution and processing parameters (laser power and scan speed) [7,11,12].

The inclusion of nanomaterials into polymers has the potential to provide performance benefits improving part quality and offering new applications [8]. However, the dispersion of the nanomaterials still remains a critical issue for the preparation of Laser Sintered

---

nanocomposites [13]. Poor interaction between polymers (organics) and nanofillers (e.g. nanoclays) leads to a nanoparticle micro-aggregation phenomenon and is a key issue for the mechanical properties [14]. Aggregated nanoclays can be expected to improve polymer rigidity but reduce toughness and elongation [15]. Here, we exploit the potential of plasma treatment to address the poor dispersion of the nanoclay in the polymer matrix.

Layered silicate based nanomaterials have attracted great interest in the field of polymer nanocomposites due to their significant impact on the intrinsic properties of the polymer matrix. The smectite mineral clay group of phyllosilicates family has been widely used in industry since the mid-nineteenth century [16]. Montmorillonite (MMT), saponite (SP), and hectorite (HT) and other uncommon species are all listed in the smectite group, and montmorillonite ($[Al_{1.67}$ $Mg_{0.33}(Na_{0.33})]$ $Si_4O_{10}(OH)_2$) [17] is the most widely used clay for reinforcing polymers. The mineral montmorillonite is composed of octahedral sheet (silica) sandwiched between two tetrahedral sheet (alumina) to form the most familiar 2:1 structure. The chemical structures, physical specifications and uses of the smectite group and other layered silicate clays are well-detailed in the literature [18–21]. Natural montmorillonite is a hydrous phyllosilicate with a negatively charged layer caused by the substitution of silicon with aluminum in the tetrahedral layer and the replacement of aluminum with magnesium in the octahedral layer. The negative charge is neutralised by mineral cations such as sodium, calcium or potassium resulting in a regular stack of tetrahedral-dioctahedral layers. The pristine montmorillonite clay is hydrophilic in nature and is consequently immiscible with hydrophobic polymers such polyamides [14]. A chemical surfactant is commonly used to increase the interlayer space (gallery) and render the hydrophilic into organophilic clay, in which the interlayer cations Na^+ or Ca^{+2} are exchanged by an alkylammonium surfactant [22,23]. This organomodification, however, is a time-consuming method [24]. In addition, organoclay platelets aggregate to form microscale tactoids, resulting in weak properties. Breaking up these aggregates into small sized tactoids or individual platelets requires further expensive or elaborate modifications. Montmorillonite can also be subjected to acid treatments with sulphuric acid (H_2SO_4) [25] or hydrochloric acid (HCl) leading to varying modifications [26]. Such treatments require special conditions to avoid any unacceptable increases of nanoclay acidity.

Therefore, this study aims to avoid the chemical techniques described previously, and to investigate a cheap, simple, and dry (chemical and water free) method for the modification of montmorillonite based nanoclays by Low Pressure Air Plasma Treatment (LP-PT) of composite powders in laser sintering applications. Although some studies on treating the clay/nanoclay (modified or nonmodified) for the reinforcement of polymers were previously carried out [27–29], plasma treatment in laser sintering applications is in its infancy [30]. Here we show for the first time that LP-PT of Nanomer (I.34TCN) clay can strongly improve the surface quality of clay/PA12 composite parts fabricated by LS. Thus, this is a unique study on the use of plasma treatment in LS applications, demonstrating for the first time that plasma treatment has the potential to provide crucial performance benefits for laser sintered nanocomposites.

2. Materials and materials processing and preparation

2.1. Nanoclays

Two different layered silicates clays were used: Cloisite 30B (C30B) (purchased from Southern Clay products, USA) and Nanomer (I.34TCN) (provided by Sigma Aldrich chemicals, UK). C30B and I.34TCN are montmorillonite-based nanoclays, organomodified with surfactants. The chemical structure and technical information of the surfactants are given in Table 1. C30B and I.34TCN were selected because they only differ in the structure of the surfactant. The alkyl ammonium salt of the C30B surfactant has a single alkyl tallow whereas two alkyl tallows are

Table 1
Surfactants information and specification (according to the suppliers' technical sheets and Ref. [32,36]).

Clay	Surfactant	Chemical Structure	Content
C30B	Methyl bis-2 hydroxyethyl tallow alkyl quaternary ammonium chloride: $[(HE)_2 M_1 T_1]$ HE: Hydroxyethyl M: Methyl (T) Tallow: $CH_2(CH_2)_{11-15}(CH=CH)_{0.5}CH_3$	$CH_3 - N^+ - T$, with CH_2CH_2OH groups	25-30 %
I.34TCN	Methyl dihydroxyethyl hydrogenated tallow ammonium chloride: $[(HE)_2 M_1 HT_1]$ HE: Hydroxyethyl M: Methyl (HT) Hydrogenated Tallow: $CH_2(CH_2)_{12-16}CH_3$	$CH_3 - N^+ - HT$, with CH_2CH_2OH groups	25-30 %

The chemical composition of the Tallow (T) is: 65% C18, 30% C16, and 5% C14. N^+: Quaternary ammonium salt.

used to treat the I.34TCN [31]. However, both surfactants possess a hydroxyl group which may lead to the formation of a hydrogen bond between the hydroxyl group in the surfactant and the polyamide (possessing a polar nature) resulting in a strong interaction between the organic polyamide and organomodified clays [32]. However, C30B and I.34TCN with the dihydroxyl-surfactant are more likely to suffer decomposition via the Hofmann elimination reaction [33,34], catalysing the degradation of polymer matrix [14,35].

2.2. Low pressure air plasma treatment (LP-PT) technique

C30B and I.34TCN were subjected to a plasma treatment using a Low-Pressure Plasma Cleaner Zepto (from Diener Electronics) using ambient air as process gas. A small quantity (< 1 g) of the nanoclay powder was placed as a thin layer in a small glass petri dish. Three petri dishes were then placed inside a cylindrical glass vacuum chamber of the plasma instrument. After evacuating the chamber to a pressure of 0.3 mbar, the plasma was generated using a power (100 W) for 1000s. As only the top-layers of the powder bed in the petri dish are exposed to the plasma, the powder was then turned half way through the stated treatment time. This procedure was repeated twice before the treated powder was then removed from the dishes and kept it in a sealed glass jar.

2.3. Materials preparation for Downward Heat Sintering (DHS) and laser sintering (LS) applications

Polyamide 12 (PA12), used as a polymer matrix, were supplied by e-Manufacturing Solutions (EOS) with a trade name of PA2200. As received PA12 is a thermoplastic and semicrystalline polymer and its chemical formula is $(C_{12}H_{23}NO)_n$. Powders (polymers and nanoclays) were mechanically mixed and ultrasonicated prior to sample production via melting (using DHS) or sintering (using LS) processes. Mixing, sonication conditions and material amounts for both processes are found in Table 2.

The composite materials of PA12 and C30B nanoclay (treated and untreated) were prepared for DHS method as described in [30]. Briefly, a simple, fast, low-cost and without any applied external pressure method was used to replicate the LS technique by means of a hot press. In the hot press, HS parts were fabricated by supplying heat from the top to powders (PA12 and C30B composites) which were preheated to below its melting temperature (temperatures and other parameters are listed in Table 2). HS parts left to cool at room temperature before collection. The processing parameters and temperatures described in [30] were optimised via our method through DSC–HSM.

Table 2
Laser and Heat Sintering processes parameters.

Clay	Materials weight[*]	Process	Parameters
C30B	50-100 g of PA12 3% and 5% plasma treated C30B and untreated C30B	Downward Heat Sintering (DHS) (30 min. mixing and 30 min. sonicating before sintering)	DHS carried out in a hot press under the following parameters[**]: PreT 185 °C for all DHS samples (15 min.) PA12: AppT 190 °C (15 min.) Plasma treated C30B/PA12 composite: AppT 192 °C (15 min.) Untreated C30B/PA12 composite: AppT 195 °C (15 min.)
I.34TCN	3kg of PA12 3% plasma treated I.34TCN and untreated I.34TCN	Laser Sintering (LS) (1 hr. mixing and 30 min. sonicating before sintering)	LS parameters are the same for all samples as follows: CO_2 laser with a wavelength of 10.6 µm; Bed temperature 172 °C; laser power (energy density[***]) 13 W (0.208 J/mm^3), 17 W (0.272 J/mm^3) and 21 W (0.336 J/mm^3); laser speed scan 2500 mm/sec; layer thickness 0.1 mm and scan spacing 0.25 mm. Under Nitrogen environment.

* Materials weight is a minimum one set of samples.
** PreT-Preheating temperature (The hot press lower part temperature); and AppT-Applied temperature (The hot press upper Part Temperature).
*** The energy densities were determined according to equation developed by Kruth et al [37].

Herein, the treated and untreated I.34TCN composites were prepared for LS applications. LS Parts from those materials (PA12 and I.34TCN composites) were produced horizontally (x and y are the layer directions) at three different laser powers (i.e. 13, 17, and 21 W) as shown in Figure S1(a) in Supplementary Information. Other LS parameters are mentioned in Table 2. The commercial LS system used for these purposes is Formiga P100 from EOS. PA12 and PA12/I.34TCN powder composites were tested to investigate the powder processing window and particle distribution as shown in Table S1 in Supplementary Information.

In summary, these investigations revealed no significant change in the morphological and thermal properties of the composite powders. Particle sizes of composite powder were slightly reduced at 10%, 50% and 90% compared to the PA12 powder due to the high-speed rotation mixing process used in this study. DSC results, showed that the difference between melting and crystallisation temperatures of PA12 was only slightly changed after incorporation of untreated and treated I.34TCN nanoclay.

3. Materials characterisation and testing

3.1. Scanning electron microscopy (SEM) and hot stage microscopy (HSM)

A Low Voltage Scanning Electron Microscopy Nova NanoSEM was used for the morphological observation of the clays before and after plasma treatment and LS cross sections produced using PA12 composites with both the treated and untreated nanoclays. An electron beam with low landing energy (2.2 KeV) was used to reduce specimen surface charging and damage. Note that no metal coating was applied to the polymer surface. Secondary electron images were collected with a Through-Lens-Detector (TLD) and a Concentric Back Scatter (CBS) detector was used for higher magnification imaging and with some chemical contrast.

High resolution SEM imaging was performed using a Helios Nanolab G3 UC microscope specifically designed for ultrahigh resolution at low voltages (< 1KV). Unlike ordinary SEM analysis, no conductive coating was deposited onto the samples. An accelerating voltage of 1.3 KV, typical vacuum pressure = 10^{-6} mbar, current = 25 pA and a working distance of 4 mm was used. The design of the in-lens detector of this SEM allows the filtering of secondary electron (SE) energy ranges so that only SE below 6 eV are allowed to form the micrographs. This technique has been confirmed to remove the effects of topography [38] and allows the high-resolution imaging of the nanoclay within the composite.

HSM is a promising technique for visualising the coalescence of particles under heating for LS applications. Additionally, this technique allows the direct visualisation of nanoclay particles during the coalescence of the polymer particles. The HSM used here is composed of a BX50 light microscope from Olympus attached to a temperature

controlled microscope stage from Linkam. Powders were melted from room temperature to 250 °C at a rate of 10 °C/min in order to be comparable with DSC profiles.

3.2. Fourier transform infrared spectroscopy (FTIR)

To explore the clays' structural and chemical composition changes during the plasma treatments, FTIR spectra was obtained using PerkinElmer Frontier spectrophotometer equipped with a Golden Gate™-single reflection Diamond ATR accessory. FTIR measurements were carried out on nanoclays, C30B and I.34TCN (without KBr dilution) by recording 10 scans in the wavenumber range from 400 to 4000 cm^{-1} at a spectral resolution of 4 cm^{-1}. Before obtaining spectra from the samples, a background spectrum with no sample was taken as a control.

3.3. Thermogravimetric analysis (TGA)

The thermal stability and thermal decomposition temperatures of the treated and untreated clays were determined with a Thermogravimetric Analyser (Pyris 1 TGA from PerkinElmer). This is because the organoclay modified with alkylammonium can have two opposing effects on the polymer and composites: i) a barrier effect resulting in an improvement of the thermal stability; ii) a catalytic effect on the decomposition of the polymer [14]. Thus, it is necessary to investigate the thermal properties of the nanoclay with and without plasma treatment before adding to the polymer matrix. The clay powder was heatedin a nitrogen environment, from 30 °C to 630 °C with a heating rate of 10 °C/min.

3.4. Tensile tests

Tensile tests were carried out on LS samples using a Tinius Olsen H5KS tensile testing machine fitted with a laser extensometer as shown in Figure S1(b) in Supplementary Information. Ultimate stress and strain, and elastic modulus were measured using the Horizon Software. The tensile tests were carried out under the conditions: speed 5 mm/min, preload 5 N and maximum load cell 5 kN. Figure S1(c) shows a schematic illustration of a standard tensile test specimen based on the ASTM D638-02a standard.

4. Results and discussion

4.1. Characterisation analysis and results

4.1.1. SEM images

The SEM micrographs of the nanoclays C30B and I.34TCN before and after plasma treatment are shown in Fig. 1(a&b) and(c&d) respectively. C30B nanoclay exhibited a reduction in agglomeration due
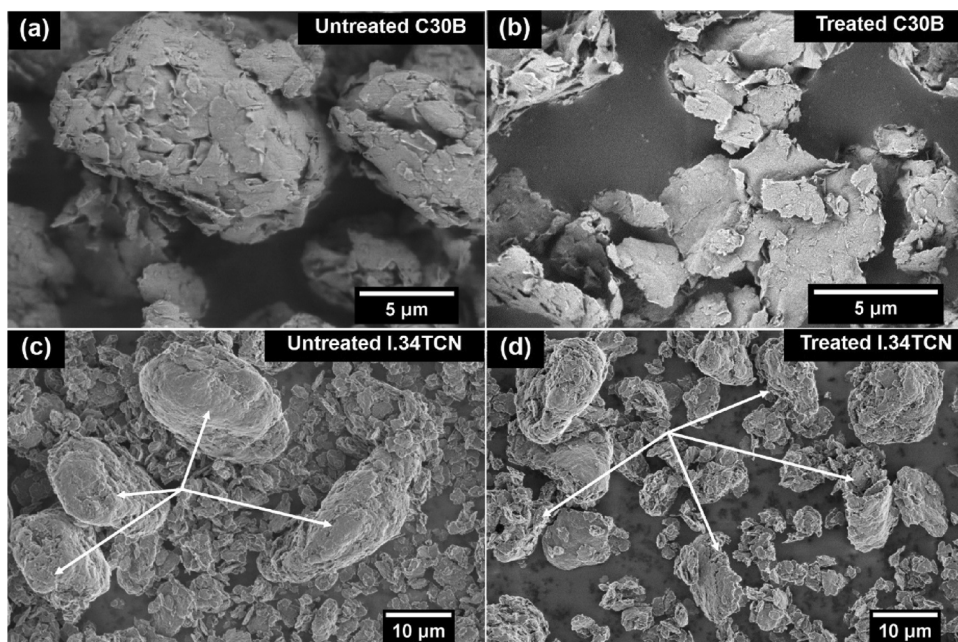
Fig. 1. Micrographs of the nanoclays before and after plasma treatment (a) untreated C30B, (b) treated C30B which are reproduced from [30] under CC-BY-4, (c) untreated I.34TCN, and (d) treated I.34TCN. Arrows in (c) refer to the large, round untreated particles, whereas in (d) they refer to particles were broken in to smaller particles during plasma treatment.

to the action of the plasma, as displayed in SEM images (using a high resolution CBS detector) in Fig. 1(a&b). Fig. 1(a) shows the NT-C30B platelets aggregated to form large and round particles of several microns. In contrast, after LP-PT thin separate sheets of clay can be seen in Fig. 1(b).

As noted Fig. 1c, the untreated I.34TCN nano-platelets were conjoined in micron-size irregular shaped particles. Some of the aggregated particles are relatively large and round or oval in shape (highlighted by arrows in Fig. 1(d) and thus, a poor micro and nano dispersion within the polymer matrix is expected [39,40]. LP-PT of clay I.34TCN (Fig. 1(d)) tended to reduce the agglomerate size to form more open, smaller agglomerates (highlighted by arrows) with visible small holes, confirming the particles responded to the plasma treatment.

These observations were also confirmed by the HSM images in Figure S2 (a and b) during heating of PA12 particles. After PA12 powder coalescence, the untreated I.34TCN particles were aggregated in relatively large nonuniform particles (examples highlighted by red arrows) reducing the contact area which may ultimately adversely affect the properties of the final parts. However, a few dispersed untreated clay particles can also be seen in Figure S2(a) which are highlighted by light green arrows. Whilst, the treated I.34TCN particles were well-dispersed (highlighted by light green arrows in Figure S2(b)) and reduced agglomerations, and this resulted in an increase of the contact area and improved the interaction between the clay and polymer matrix. Ultimately, this effect is expected to improve the properties of the final products. Some small aggregated treated clay particles were observed and highlighted by red arrows.

4.1.2. FTIR analysis

Fig. 2(a&b) shows the FTIR spectra of untreated and plasma treated nanoclays C30B and I.34TCN respectively, with the major absorption bands positions outlined in four regions. It can be observed that the untreated C30B and untreated I.34TCN nanoclays displayed similar patterns and the intensity of the peaks were approximately the same. The FTIR spectra of C30B and I.34TCN in Fig. 2(a(a&b) display inorganic montmorillonite peaks at wavenumbers $\sim 990\,cm^{-1}$ and $\sim 1116\,cm^{-1}$ which are related to the stretching vibrations of Si-O-Si and Si-O respectively, $\sim 1640\,cm^{-1}$ is assigned to O−H bending, and $\sim 3360\,cm^{-1}$ and $\sim 3626\,cm^{-1}$ correspond to O−H stretching for the adsorbed water and the silicate [33–41].

In addition, the organic surfactant has displayed peaks attributed to

the C–H vibration at $\sim 1470\,cm^{-1}$ (bending) and two adjacent peaks at $\sim 2852\,cm^{-1}$ and $\sim 2926\,cm^{-1}$ (symmetric and asymmetric stretching) [33–41]. The wide wavenumber range in Fig. 2 reveals that the strongest peak appeared at $990\,cm^{-1}$. Further changes can be seen in the range of (1200-2000 cm^{-1} and 3250-3750 cm^{-1}) as shown in Fig. 3.

As observed, a reduction in the intensity of the Si-O-Si peak related to the spectra of C30B and I.34TCN (Fig. 3(a&d)) which is coupled with an intensity change of the peak located at $\sim 3626\,cm^{-1}$ (hydroxyl stretching) in Fig. 3(c&f) confirmed that the LP−PT has made structural changes in the mineral portion (MMT) of the organoclays. It is suggested that the chemical change is attributed to a partial breakdown of the surface silicate with a formation of a new hydroxyl [28]. The broad peak centred around $\sim 3360\,cm^{-1}$ corresponding with adsorbed water also decreased in the C30B and I.34TCN spectra, as shown in Fig. 3(c&f), this could be due to the increased temperature within the plasma chamber. The influence of the plasma on the nanoclays' organic surfactants is observed as the peak associated with C–H bending ($\sim 1470\,cm^{-1}$) decreased and a peak at $\sim 1695\,cm^{-1}$ owing to the carboxylic acid [33] has become more intense [42]. In addition, the two adjacent peaks at $\sim 2852\,cm^{-1}$ and $\sim 2926\,cm^{-1}$ assigned to symmetric and asymmetric C–H stretching of the organic surfactant of C30B and I.34TCN also decreased as shown in Fig. 3(b&e).

4.1.3. Thermogravimetric analysis (TGA) results

Fig. 4(a&b) shows the TGA thermograms of the untreated and plasma treated C30B and I.34TCN, respectively. Generally, the organic modified nanoclays decompose in four steps: (i) desorption of water (loss of free water) below 200 °C, and dehydration of hydrated cations (loss of the interlayer hydration water only if there is some unexchanged Na^+ ions); (ii) decomposition of the organic surfactant, in the range 200 °C–500 °C; (iii) dihydroxylation of MMT (structural water) in the temperature range 500–800 °C and finally (iv) organic carbon reactions above 800 °C [22,43,44]. As shown in Fig. 4, the decomposition patterns of the untreated and plasma treated nanoclays (treated C30B and treated I.34TCN) are similar. However, the plasma treated C30B and I.34TCN exhibited higher decomposition temperature than the untreated ones at all the degradation steps.

For a deeper insight, the decomposition temperatures at onset point (5%) and 10% and of the untreated and plasma treated C30B and I.34TCN obtained from Fig. 4, are summarised in inset Tables i and ii. The first observation is that, at the early stage degradation (below
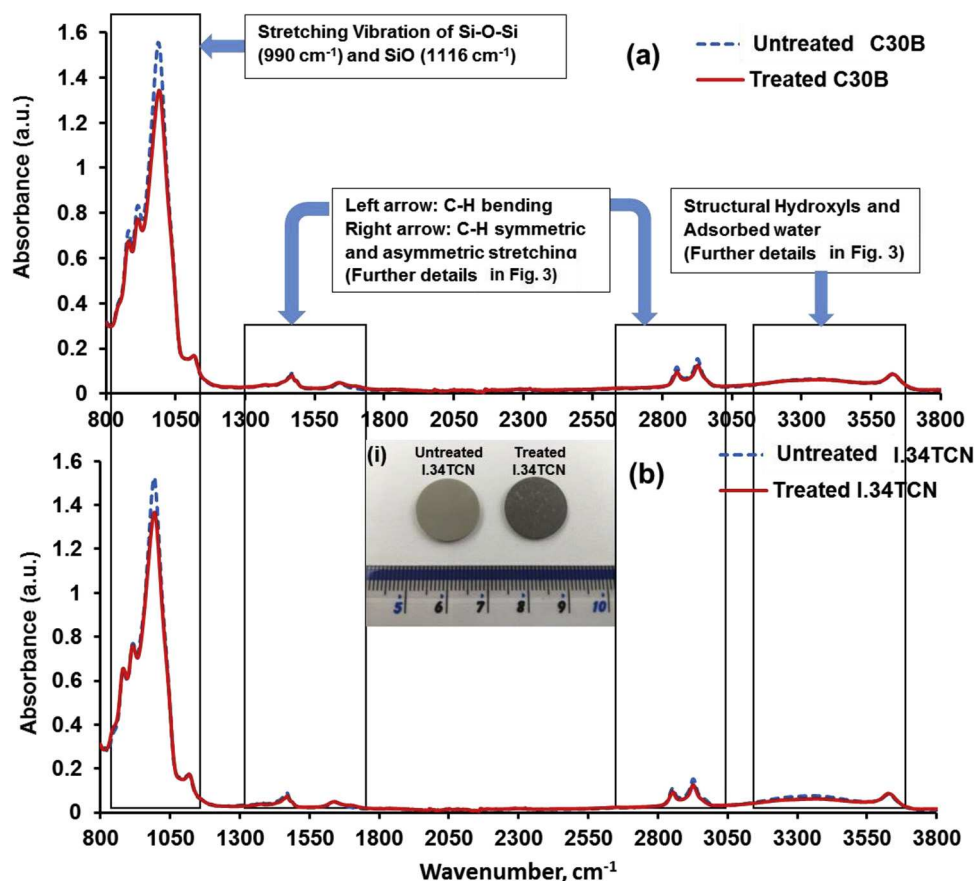
Fig. 2. FTIR spectra of untreated and plasma treated nanoclays (a) C30B (reproduced from [30] under CC-BY-4), (b) I.34TCN; Pressed discs of the untreated and treated I.34TCN powders pictured in inset (i) shows a clear change in color after air plasma.

200 °C), the difference in the decomposition temperature between the untreated C30B and I.34TCN is limited (5 °C at 5% weight loss) compared to the degradation at higher temperatures (such as at 10% the difference 20.9 °C) of the untreated nanoclays' degradation patterns. It is attributed to the fact that the region at the temperature below 200 °C is assigned mostly to the free water (and possibly interlayer water loss) in which the organoclays are expected to have a similar water content [44]. In contrast, above 200 °C the organic surfactant is the main degraded substance [44] and, as mentioned earlier in this study, the organic surfactants of C30B and Nanomer I.34TCN are not the same since C30B surfactant has a single alkyl tallow whereas I.34TCN has two alkyl tallows. Thus, as can be seen in inset Tables in Fig. 4, the decomposition temperature of I.34TCN is higher than those of C30B at the temperature where the organic substance is involved. In addition, the plasma shifts the decomposition temperatures of C30B and I.34TCN to higher values at all steps as shown in Fig. 4, and inset Tables. This plays a critical role in maintaining the thermal stabilisation of the composite powder at higher temperature or laser power for the LS fabricated parts and even to the surrounding powder for the recovering process.

We suggest that the above TGA results coupled with the FTIR analysis shows that the plasma results in two actions i) the improvement of the thermal stability of the organoclays C30B and I.34TCN and ii) the formation of a new hydroxyl at the surface of the MMT converting carbons from the alkylic tail to carboxyl [42].

4.1.4. Influence of plasma treatment on the quality of Laser sintered parts

In our previous works [30,45], the organonanoclay C30B (treated and untreated) was used to reinforce the PA12 using a new, simple and cheap fabrication method: Downward Heating Sintering (DHS). Previous work [30] aimed to replicate the laser sintering process whilst minimising powder waste as DHS method requires 50–100 grams

compared to the typical 3 kg required by LS. As noted earlier, both C30B and I.34TCN are almost similar since both are MMT-based nanoclays modified by dihydroxyl alkyl ammonium organic surfactant. Moreover, these thermal investigations showed that the I.34TCN are more thermally stable than C30B. Hence, I.34TCN was the only nanoclay used for the following used for LS investigations.

DHS was used to determine LS parameters [30], which were then used to fabricate the PA12 and composites (3% untreated I.34TCN and 3% treated I.34TCN). Different samples with different shapes and complexities were built successfully by LS as shown in Fig. 5. Visual inspection showed that there was no shrinkage or failed complex shapes for all of the built objects. The colour of LS samples is as follows: neat PA12 -white; untreated I.34TCN composite -light beige and treated I.34TCN composite -light grey. The colour differences imply that the plasma treatment of nanoclay affects the nanocomposite formation during LS.

The microstructure of cross-sectioned LS parts (bed temperature 172 °C and laser power 21 W) built from neat PA12, untreated and treated I.34TCN composites obtained by SEM are shown in Fig. 6. The surface morphology of two different areas of each specimen were investigated: top left and middle sections of neat PA12 (Fig. 6(a) and (b)), untreated I.34TCN composite (Fig. 6(c) and (d)) and treated I.34TCN composite (Fig. 6(e), and (f)). The fracture surface of the PA12 sample displays various irregular pores. Enlarged internal pores are surrounded by un-melted or partially melted particles on the edges of the part. Heterogeneous rough and porous surfaces are also observed in areas far from the edges of the part as shown in Fig. 6(b), with the elongated shape of the pores potentially demonstrating some ductile fracture.

The incorporation of nanoclay (untreated and treated I.34TCN) has altered the surface morphologies (see Fig. 6(c–f)) where relatively flat and uniform cross sections are observed. Micro-holes and cracks were
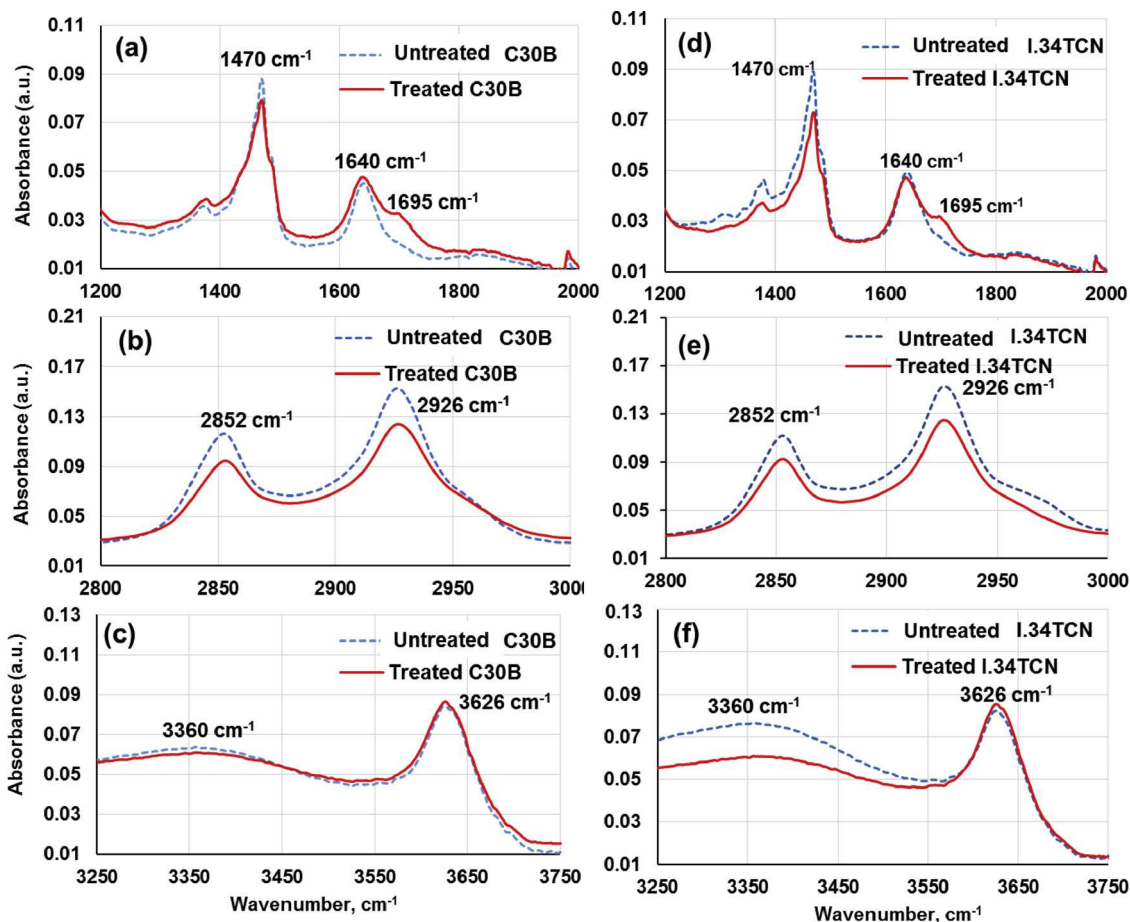
Fig. 3. FTIR spectra of untreated and treated nanoclays (a–c) C30B (reproduced from [30] under CC-BY-4) and (d–f) I.34TCN.

(i) Cloisite 30B		
	Nontreated	Treated
Weight loss %	Decomposition temperature	
5%	275.7 °C	282.3 °C
10%	314.6 °C	344.7 °C

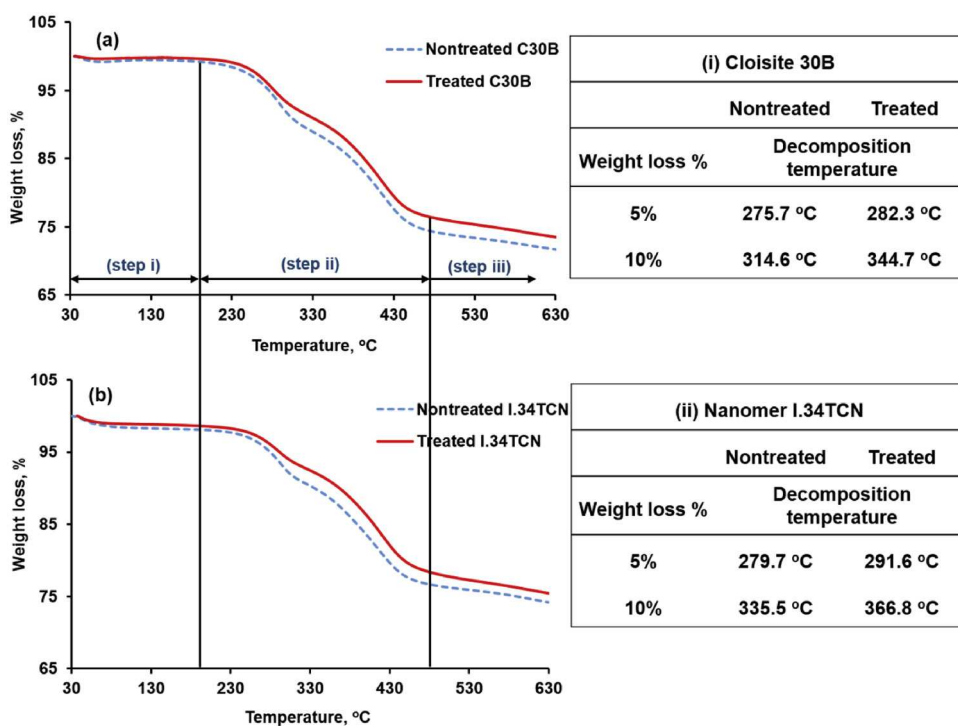| (ii) Nanomer I.34TCN		
	Nontreated	Treated
Weight loss %	Decomposition temperature	
5%	279.7 °C	291.6 °C
10%	335.5 °C	366.8 °C

Fig. 4. TGA thermograms of untreated and plasma treated nanoclays (a) C30B (reproduced from [30] under CC-BY-4), (b) I.34TCN. Inset Tables (i) and (ii) are the decomposition temperatures of untreated and plasma treated C30B and I.34TCN.
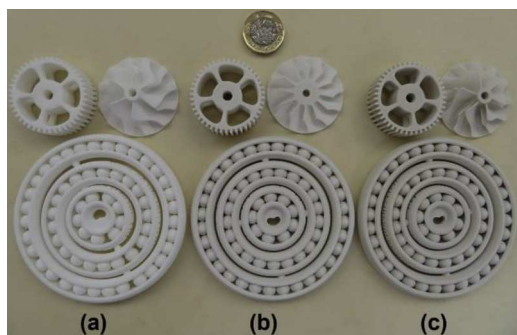
Fig. 5. Different shaped-LS samples (a) Neat PA12, (b) 3% untreated I.34TCN composite and (c) 3% plasma treated I.34TCN composite.

also observed in Fig. 6(c–f) (marked by arrows) which are attributed to the interlayer spaces or voids generated by adjacent particles that did not fuse completely [46]. However, the composite containing the treated I.34TCN (Fig. 6(e)) reveals a more uniform surface than the untreated I.34TCN composite shown in Fig. 6(c). Moreover, the former fracture surface has smaller sized micro-pores and fewer unmelted/partly melted particles than the fracture surface of the composite containing the untreated I.34TCN (Fig. 6(c)). Furthermore, larger cracks were observed in the untreated I.34TCN composite specimen (Fig. 6(d)) whilst the treated I.34TCN composite (Fig. 6(f)) has relatively few pores compared to the untreated one in parallel zones. This suggests that the

interaction between the LP-PT treated nanoclay (treated I.34TCN) and polymer (PA12) (reflected by the color change of the composite parts) may facilitate the flowability of the nanocomposite powders. In addition, the well-dispersed plasma treated I.34TCN particles in PA12 could potentially enhance laser energy absorption during sintering.

Cross-sectional SEM images near edges in Figure S3(a) in Supplementary Information (untreated I.34TCN composite) and Figure S3(b) (treated I.34TCN composite) show the following main features: unmelted particles (rougher surface); partially melted particles (smooth surface and neck formation); micro-pores and sintered regions (similar observations were also reported [7,46]).

As the LS is a mould-less powder casting system, it is possible the particles at the boundaries have not received sufficient energy for sintering resulting in non or partially melted particles at the part edges. Similarly, to the inhomogeneity in the untreated composite powder before sintering [30], untreated I.34TCN aggregated particles can be easily seen on the non-melted PA12 particles (highlighted by circles in Figure S3(a)) whereas the absence of visible clay aggregates in Figure S3(b) suggest efficient incorporation of clay into the polymer matrix. High resolution images at high magnification (1 μm or less) were collected to discuss the nanoclay dispersion in the polymer matrix in next section.

The well dispersed clay has been shown to influence melt and crystallisation [47] which is consistent with improved melt behaviour here as evidenced by the smooth surface in Figure S3(b). The uniformly dispersed plasma treated nanoclay could act as a nucleation centre
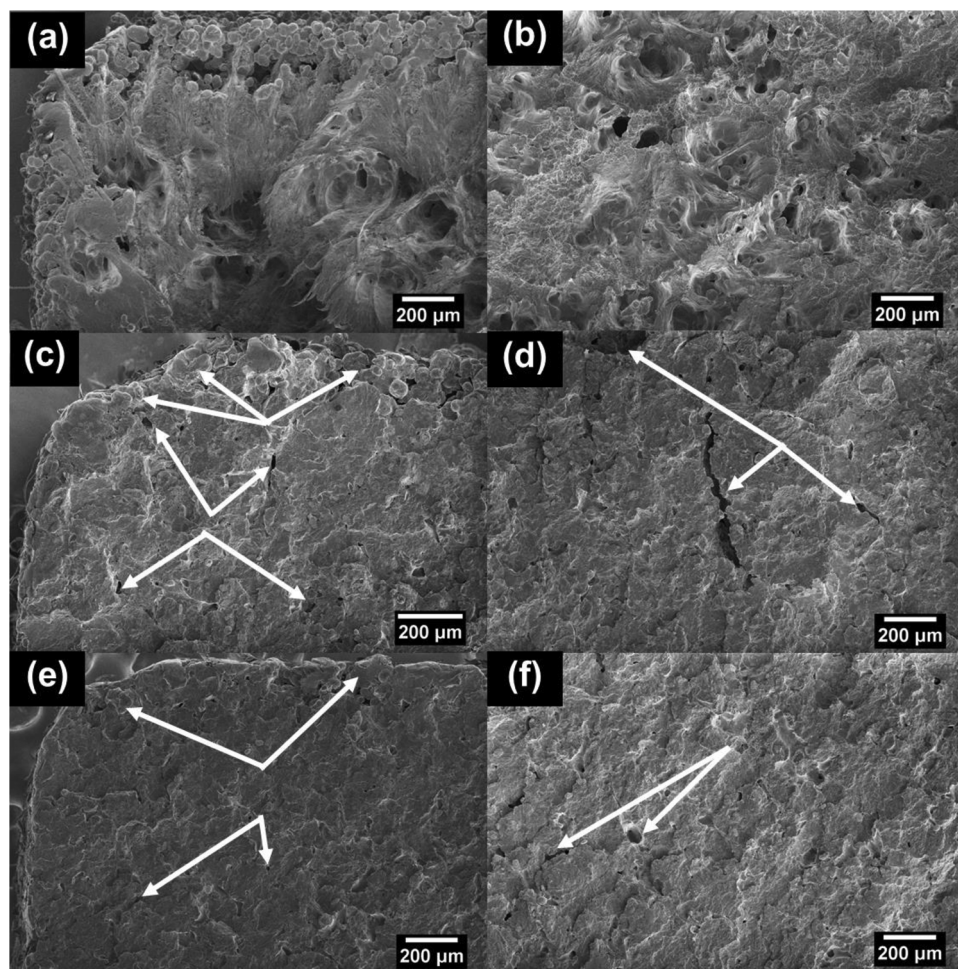

Fig. 6. Cross-sectional SEM images of the LS specimen (a–b) neat PA12, (c–d) untreated I.34TCN composite (e–f) treated I.34TCN composite. Images on the left display the top left edge of the composites (Area 1 in Figure S1(d)) whilst the images on the right are of the middle regions (Area 2 in Figure S1(d)). The white arrows highlight cracks and pores.
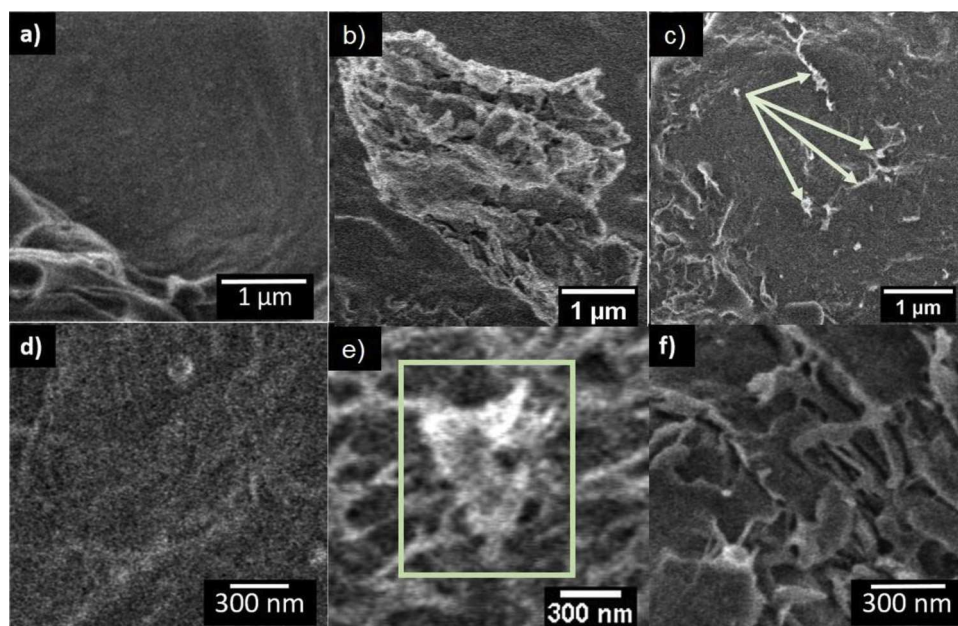
Fig. 7. High resolution low voltage SEM imaging of fractured surfaces of a) PA12, b) untreated I.34TCN composite, and c) treated I.34TCN composite on the micron scale and d) PA12, e) untreated I.34TCN composite, and f) treated I.34TCN composite on the nanoscale.

during the crystallisation of the polymer matrix [48]. In contrast, untreated nanoclay shows island-like aggregations [13] as shown in Figure S3(a). However, a further investigation on the exact mechanism of nanoclay incorporation on the surface morphology of the LS parts is required if this effect is to be exploited for improved surface quality or mechanical properties of LS produced parts.

4.2. Dispersion of I.34TCN (untreated and plasma treated) in PA12

Fig. 7 shows the SEM micrographs illustrating the morphologies of PA12 (Fig. 7(a&d)), untreated I.34TCN composite (Fig. 7b&e) and treated I.34TCN composite (Fig. 7c&f) cross sections. TiO_2 nanoparticles were observed on PA12 polymeric surface as shown in Fig. 7(a) and (d) which has been discussed in our previous study [49]. Further analysis about these observations are inserted in Supplementary Information, Figure S4. The inhomogeneity of the untreated nanoclay can be easily observed in Fig. 7(b) and (e) (Full-scale SEM images of Fig. 7(b) and (e) are available in Supplementary Information, Figure S5a and Figure S5b respectively). The nanoclay particles were aggregated on the micro-scale in a flat surface area like in Fig. 7(b) and nanoscale aggregates were observed in a plastically deformed area such as in Fig. 7(e). Some of the islands of untreated I.34TCN, found on nonmelted particles in Figure S3a, are observed to have broken-up under tension to smaller aggregates of a few microns in size or less on the PA12 surface, for example Figure S6 in Supplementary Information.

An area is more likely to promote a brittle fracture shown Figure S7 in the Supplementary Information, displayed a relatively flat and aggregated nanoclay platelets. On the other hand, the advantageous effect of the LP−PT is shown by the improvement in dispersion of the nanoclay into PA12 was observed in Fig. 7(c) and (f) (Full-scale SEM image of Fig. 7(c) and (f) are available in Supplementary Information, Figure S5(c) and Figure S5(d) respectively). The plasma treated nanoclay platelets (Fig. 7(c)) are randomly distributed and less aggregated than the untreated ones (Fig. 7(b)) even though the region was flat. The treated particle sizes were remarkably reduced (highlighted by arrows in Fig. 7(c)) and were dispersed more efficiently than untreated particles shown in Fig. 7(b). The nanoscale SEM image in Fig. 7(e) was taken on a plastically deformed region, reveals that the treated nanoclay was dispersed in-between the PA12 layers as nanosized thin sheets and

oriented toward the cross section. However, some of these nanosheets had a poor interfacial bonding with PA12 in one side of these sheets as observed in Fig. 7(f). This poor cohesion in parts of the composite structure may limit the advantageous effect of the nanoclay [50]. Hence, a further optimisation of the plasma treatment is required for a better interfacial bonding. These SEM observations and results are linked to the mechanical behaviour of the PA12 composites in the next section.

To conclude the SEM observations, the plasma treatment reduced the micro-aggregation and improved the dispersion of the nanoclay leading, to some extent, to a partially exfoliated structure in some regions and partially intercalated structure in other regions. This confirms the critical role of the plasma treatment for successful nanocomposite formation.

4.3. Mechanical properties

The tensile test (Ultimate Stress, Ultimate Strain and Elastic Modulus) results obtained from the LS samples of the PA12 and its composites (untreated I.34TCN composite and treated I.34TCN
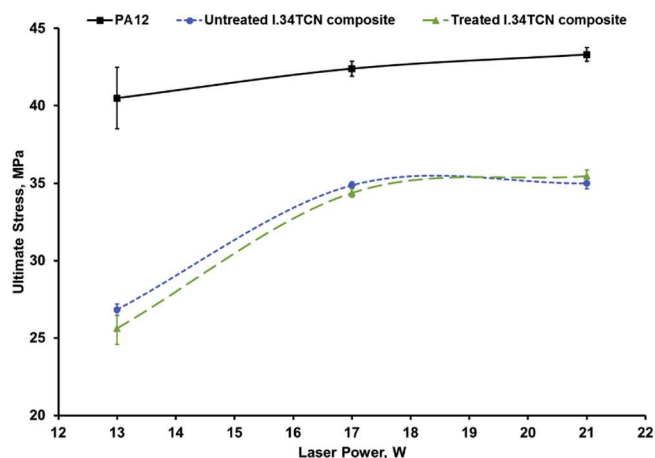

Fig. 8. Ultimate stress results obtained from PA12, untreated I.34TCN and treated I.34TCN composites at three different laser powers: 13, 17, and 21 W.
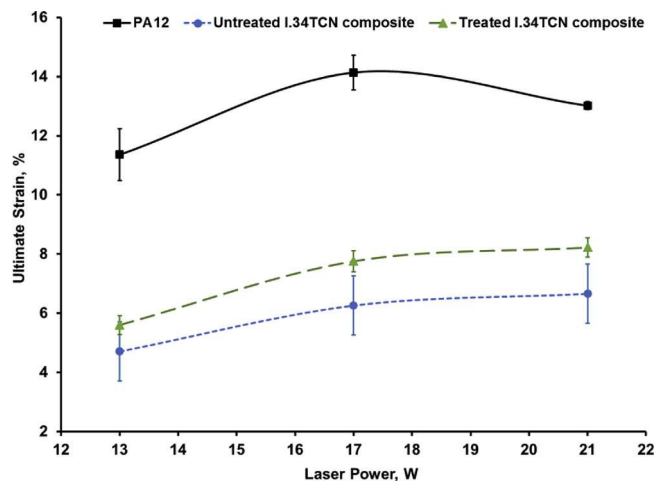
Fig. 9. Ultimate strain results obtained from PA12, untreated I.34TCN composite and treated I.34TCN composite at three different laser powers: 13, 17, and 21 W.
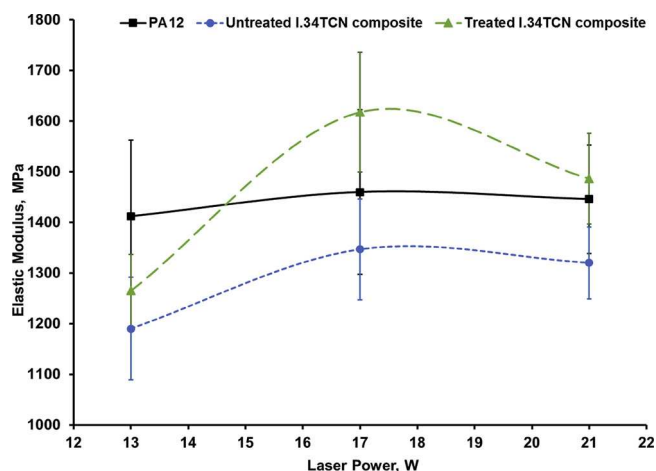

Fig. 10. Elastic modulus results obtained from PA12, untreated I.34TCN composite and treated I.34TCN composite at three different laser power: 13, 17, and 21 W.

composite) are shown in Figs. 8–10. The ultimate stress of PA12 linearly increased with increasing laser power from 40.49 ± 1.99 MPa at 13 W to 42.40 ± 0.49 MPa at 17 W and then to 43.30 ± 0.44 MPa at 21 W. Whilst the measured ultimate strain increased from 11.36% ± 0.87 reaching maximum values of 14.13 ± 0.58% at 17 W and then decreased to 13.02 ± 0.13% at 21 W.

The ultimate stress and strain of the PA12 composites (untreated and treated) both demonstrated a different trend compared to that of neat PA12. The ultimate stress of the untreated I.34TCN composite and treated I.34TCN composite was remarkably increased from 26.83 ± 0.35 MPa and 25.62 ± 1.05 MPa at 13 W to 34.88 ± 0.22 MPa and 34.37 ± 0.26 MPa at 17 W and a limited increase to 35 ± 3.7 MPa and 35.45 ± 0.40 MPa by increasing the laser power to 21 W. The ultimate strain, on the other hand, of untreated I.34TCN composite and treated I.34TCN composite increased from 4.71 ± 0.13 MPa and 5.6 ± 0.32 MPa at 13 W to 6.27 ± 0.13 MPa and 7.76 ± 0.36 MPa at 17 W and then to 6.66 ± 0.25 MPa and 8.23 ± 0.32 MPa at 21 W.

As can be seen, in each case the UT-Stress of plasma treated, and untreated composites were lower than that for PA12, and more dramatically so at lower laser powers (Fig. 8). Also treated vs untreated showed no effect. As expected, the UT-Strain of the untreated I.34TCN composite and treated I.34TCN composite, shown above, are substantially lower than that of the PA12 due to the addition of rigid nanoclays [51]. However, the treated I.34TCN composite show a better elongation than that obtained from the untreated I.34TCN composite samples as shown in Fig. 9. The variation in the ultimate stress values for low laser powers of the treated I.34TCN composite was smaller than that for PA12 and untreated I.34TCN composite.

All the elastic modulus results obtained from PA12, untreated I.34TCN composite, and treated I.34TCN composite started from lowest values at 13 W: 1412 ± 150.7 MPa, 1190 ± 101.4 MPa, and 1265 ± 72 MPa respectively. Then, these values increased reaching maximum values at 17 W: 1460 ± 162.9 MPa, 1346.7 ± 99.5 MPa, and 1618 ± 118.2 MPa, before decreasing at 21 W to: 1446 ± 107.1 MPa, 1320 ± 71.3 MPa, and 1486.7 ± 89.6 MPa respectively. As can be observed, at 17 W and 21 W laser powers, the elastic moduli of the treated composite exhibited higher values than those obtained from PA12 and untreated composite and the best value was obtained at laser power 17 W. In addition, the spread of data of the elastic modulus is relatively large compared to the ultimate stress and strain data at all laser power inputs in line with previous literature [1,6].

In conclusion, as expected, the poorer tensile test results of untreated I.34TCN composite Figs. 9 and 10 coupled with the non-uniform surface showed by SEM images in Fig. 6(c), Figure S3(a) and Fig. 7(b) suggest that the untreated nanoclay agglomerations absorbed higher energy causing large local variations of temperature. Therefore, some particles with poorly distributed untreated nanoclays were mostly partially melted which resulted in weak mechanical properties as reported in previous studies [14,22]. On the other hand, no signs of large agglomerations but smooth surface melt area (Figure S3(a)) and better dispersion (Fig. 7(d) and (f)) were obtained in treated I.34TCN composite. As a result, the elastic modulus of treated I.34TCN compositewas significantly improved and higher than that of PA12 and untreated I.34TCN composite at a laser power of 17 and 21 W. Although, for most materials improving stiffness are accompanied by reduction in ductility [1], the LP-PT has a beneficial effect on stiffness whilst also promoting a less brittle fracture of treated I.34TCN composite. On the other hand, the reduction in the composites toughness, shown in Fig. 8, can be attributed to the fact that a fully exfoliated structure was not achieved [52] even though, the PT composite exhibited well-dispersed nanoclay as previously discussed. This is because some region showed poor-adhesion between the plasma treated I.34TCN and PA12 (Fig. 7(f)) could lead to less interfacial reinforcing area and less resistance to nanoclay slippage. We observed that the same particle showed good adhesion one side but a poor adhesion on the other, suggesting uneven exposure to the plasma. Therefore, further work is required to optimise the processing parameters of the LS PA12 composites including the powder mixing parameters but most importantly, the plasma treatment geometry and duration.

5. Conclusion

We conclude that surface modification by air plasma exposure can be used to improve the nanoclay thermo-chemical properties and enhance the compatibility between the organic and nonorganic materials, ultimately, resulting in good processibility of complex LS composite parts, and most notably, improving the surface quality. We found the plasma treatment could improve the affinity between the nanoclay and PA12 and therefore it significantly reduced the nanoclay aggregates and improved the dispersion quality. Furthermore, LP-PT can increase laser sintered composites' stiffness and promote a reduced brittleness when plasma treated nanoclays are added instead of untreated nanoclay. Therefore, it is feasible to establish a link between plasma and Laser Sintering techniques to modify the end-use part properties, however, a further optimisation of the plasma treatment is required to fully exploit this potential.

Acknowledgements

Alaa Almansoori thanks the Ministry of Higher Education and Scientific Research (MOHESR) of Iraq and its representative in the UK, the Iraqi Attaché in London for financial support. Cornelia Rodenburg and Kerry Abrams thank the Engineering and Physical Sciences Research Council (EPSRC) for funding under EP/N008065/1. Candice Majewski would like to recognise the EPSRC Future Manufacturing Hub in Manufacture using Advanced Powder Processes (EP/P006566/1) with which this work is aligned. We also thank Wendy Birtwistle (Centre for Advanced Additive Manufacturing at The University of Sheffield) and staff of the Sorby Centre for Electron Microscopy and Microanalysis and acknowledge their support.

Appendix A. Supplementary data

Supplementary material related to this article can be found, in the online version, at doi:https://doi.org/10.1016/j.addma.2018.11.016.

References

[1] G.M. Vasquez, C.E. Majewski, B. Haworth, N. Hopkinson, A targeted material selection process for polymers in laser sintering, Addit. Manuf. 1 (2014) 127–138.
[2] D. Bourell, et al., Materials for additive manufacturing, CIRP Ann. Manuf. Technol. 66 (2) (2017) 659–681.
[3] S. Berretta, K. Evans, O. Ghita, Additive manufacture of PEEK cranial implants: manufacturing considerations versus accuracy and mechanical performance, Mater. Des. 139 (2018) 141–152.
[4] M.M. Savalani, L. Hao, P.M. Dickens, Y. Zhang, K.E. Tanner, R.A. Harris, The effects and interactions of fabrication parameters on the properties of selective laser sintered hydroxyapatite polyamide composite biomaterials, Rapid Prototyp. J. 18 (1) (2012) 16–27.
[5] S. Berretta, O. Ghita, K.E. Evans, Morphology of polymeric powders in Laser Sintering (LS): from Polyamide to new PEEK powders, Eur. Polym. J. 59 (2014) 218–229.
[6] C.E. Majewski, H. Zarringhalam, D. Toon, U. Ajoku, N. Hopkinson, M.P. Caine, The use of off-line part production to predict the tensile properties of parts produced by Selective Laser Sintering, J. Mater. Process. Technol. 209 (6) (March) (2009) 2855–2863.
[7] D.L. Bourell, T.J. Watt, D.K. Leigh, B. Fulcher, Performance limitations in polymer laser sintering, Phys. Procedia 56 (C) (2014) 147–156.
[8] A. Wegner, New polymer materials for the laser sintering process: polypropylene and others, Phys. Procedia 83 (2016) 1003–1012.
[9] S.C. Ligon, R. Liska, J. Stampfl, M. Gurr, R. Mülhaupt, Polymers for 3D printing and customized additive manufacturing, Chem. Rev. 117 (15) (2017) 10212–10290.
[10] S.A.M. Tofail, E.P. Koumoulos, A. Bandyopadhyay, S. Bose, L. O'Donoghue, C. Charitidis, Additive manufacturing: scientific and technological challenges, market uptake and opportunities, Mater. Today 21 (1) (2018) 22–37.
[11] L. Hao, M.M. Savalani, Y. Zhang, K.E. Tanner, R.A. Harris, Effects of material morphology and processing conditions on the characteristics of hydroxyapatite and high-density polyethylene biocomposites by selective laser sintering, Proc. Inst. Mech. Eng. Part L J. Mater. Des. Appl. 220 (3) (2006) 125–137.
[12] G.V. Salmoria, J.L. Leite, R.A. Paggi, The microstructural characterization of PA6/PA12 blend specimens fabricated by selective laser sintering, Polym. Test. 28 (no. 7) (2009) 746–751.
[13] P.K. Jain, P.M. Pandey, P.V.M. Rao, Selective laser sintering of clay-reinforced polyamide, Polym. Compos. 31 (4) (2010) 732–743.
[14] S. Pavlidou, C.D. Papaspyrides, A review on polymer-layered silicate nanocomposites, Prog. Polym. Sci. 33 (12) (2008) 1119–1198.
[15] P.C. Lebaron, Z. Wang, T.J. Pinnavaia, Polymer-layered silicate nanocomposites: an overview, Appl. Clay Sci. 15 (1–2) (1999) 11–29.
[16] I.E. Odom, Smectite clay minerals: properties and uses, Philos. Trans. R. Soc. A Math. Phys. Eng. Sci. 311 (1517) (1984) 391–409.
[17] L.A. Utracki, Clay-containing polymeric nanocomposites and their properties, IEEE Electr. Insul. Mag. 26 (4) (2010) 6–15.
[18] S. Sinha Ray, M. Okamoto, Polymer/layered silicate nanocomposites: a review from preparation to processing, Prog. Polym. Sci. 28 (11) (2003) 1539–1641.
[19] G. Brown, Crystal Structures of Clay Minerals and Related Phyllosilicates, Philos. Trans. R. Soc. London 311 (1517) (1984) 221–240.
[20] H.H. Murray, Traditional and new applications for kaolin, smectite and polygorskite: a general overview, Appl. Clay Sci. 17 (2000) 207–221.
[21] J. Madejová, FTIR techniques in clay mineral studies, Vib. Spectrosc. 31 (1) (2003) 1–10.
[22] Y. Xi, Z. Ding, H. He, R.L. Frost, Structure of organoclays - an X-ray diffraction and thermogravimetric analysis study, J. Colloid Interface Sci. 277 (1) (2004) 116–120.
[23] H. He, Y. Ma, J. Zhu, P. Yuan, Y. Qing, Organoclays prepared from montmorillonites with different cation exchange capacity and surfactant configuration, Appl.

[24] A. Vazquez, M. López, G. Kortaberria, L. Martín, I. Mondragon, Modification of montmorillonite with cationic surfactants. Thermal and chemical analysis including CEC determination, Appl. Clay Sci. 41 (1–2) (2008) 24–36.
[25] B. Tyagi, C.D. Chudasama, R.V. Jasra, Determination of structural modification in acid activated montmorillonite clay by FT-IR spectroscopy, Spectrochim. Acta - Part A Mol. Biomol. Spectrosc. 64 (2) May) (2006) 273–278.
[26] J. Madejová, J. Bujdák, M. Janek, P. Komadel, Comparative FT-IR study of structural modifications during acid treatment of dioctahedral smectites and hectorite, Spectrochim. Acta - Part A Mol. Biomol. Spectrosc. 54 (10) (1998) 1397–1406.
[27] K. Fatyeyeva, F. Poncin-Epaillard, Sulfur dioxide plasma treatment of the Clay (Laponite) particles, Plasma Chem. Plasma Process. 31 (3) June) (2011) 449–464.
[28] A.T. Djowe, S. Laminsi, D. Njopwouo, E. Acayanka, E.M. Gaigneaux, Surface modification of smectite clay induced by non-thermal gliding arc plasma at atmospheric pressure, Plasma Chem. Plasma Process. 33 (4) (August) (2013) 707–723.
[29] V. Skrockiene, K. Žukiene, S. Tučkute, Properties of recycled thermoplastic polyurethane filled with plasma treated bentonite, Plasma Process. Polym. 12 (11) (2015) 1284–1292.
[30] A. Almansoori, C. Majewski, C. Rodenburg, Nanoclay/Polymer composite powders for use in laser sintering applications: effects of nanoclay plasma treatment, JOM 69 (11) (2017).
[31] I.K. Yang, P.H. Tsai, Preparation and characterization of polyether-block-amide copolymer/clay nanocomposites, Polym. Eng. Sci. 47 (3) March) (2007) 235–243.
[32] Z. Zhang, J.H. Lee, S.H. Lee, S.B. Heo, C.U. Pittman, Morphology, thermal stability and rheology of poly(propylene carbonate)/organoclay nanocomposites with different pillaring agents, Polymer (Guildf). 49 (12) (2008) 2947–2956.
[33] J.M. Cervantes-Uc, J.V. Cauich-Rodríguez, H. Vázquez-Torres, L.F. Garfias-Mesías, D.R. Paul, Thermal degradation of commercially available organoclays studied by TGA-FTIR, Thermochim. Acta 457 (1–2) (2007) 92–102.
[34] C. Zhao, H. Qin, F. Gong, M. Feng, S. Zhang, M. Yang, Mechanical, thermal and flammability properties of polyethylene/clay nanocomposites, Polym. Degrad. Stab. 87 (1) (2005) 183–189.
[35] A.S. Hadj-Hamou, S. Matassi, H. Abderrahmane, F. Yahiaoui, Effect of cloisite 30B on the thermal and tensile behavior of poly(butylene adipate-co-terephthalate)/poly(vinyl chloride) nanoblends, Polym. Bull. Berl. (Berl) 71 (6) (2014) 1483–1503.
[36] E. Pérez, C.J. Pérez, V.A. Alvarez, C. Bernal, Fracture behavior of a commercial starch/polycaprolactone blend reinforced with different layered silicates, Carbohydr. Polym. 97 (2) (2013) 269–276.
[37] J.P. Kruth, B. Vandenbroucke, J.V. Vaerenbergh, I. Naert, Digital manufacturing of biocompatible metal frameworks for complex dental prostheses by means of SLS/SLM, Proceedings of the 2nd International Conference on Advanced Research and Rapid Prototyping (2005) 139–145.
[38] V. Kumar, et al., Nanoscale mapping of bromide segregation on the cross sections of complex hybrid perovskite photovoltaic films using secondary Electron hyperspectral imaging in a scanning Electron microscope, ACS Omega 2 (2017) 2126–2133.
[39] D.R. Paul, L.M. Robeson, "Polymer nanotechnology : nanocomposites," Polym. With aligned carbon Nanotub, Act. Compos. Mater. 49 (15) (2008) 3187–3204.
[40] E. Sancaktar, J. Kuznicki, International Journal of Adhesion & Adhesives Nanocomposite adhesives : mechanical behavior with nanoclay, Int. J. Adhes. Adhes. 31 (5) (2011) 286–300.
[41] R. Gu, et al., Characteristics of wood – plastic composites reinforced with organonanoclays, J. Reinf. Plast. Compos 29 (24) (2010) 3566–3586.
[42] R. Scaffaro, A. Maio, Enhancing the mechanical performance of polymer based nanocomposites by plasma-modification of nanoparticles, Polym. Test. 31 (7) (2012) 889–894.
[43] G. Edwards, P. Halley, G. Kerven, D. Martin, Thermal stability analysis of organosilicates, using solid phase microextraction techniques, Thermochim. Acta 429 (1) (2005) 13–18.
[44] W. Xie, Z. Gao, K. Liu, W. Pan, R. Vaia, Thermal characterization of organically modi ® ed montmorillonite, Thermochim. Acta 368 (2001) 0–11.
[45] A. Almansoori, R. Seabright, C. Majewski, C. Rodenburg, Feasibility of plasma treated clay in Clay/Polymer nanocomposites powders for use laser sintering (LS), IOP Conf. Ser.: Mater. Sci. Eng. 195 (1) (2017).
[46] H.C.H. Ho, W.L. Cheung, I. Gibson, Morphology and properties of selective laser sintered bisphenol a polycarbonate, Ind. Eng. Chem. Res. 42 (9) (2003) 1850–1862.
[47] T.G. Mofokeng, S.S. Ray, V. Ojijo, Influence of selectively localised nanoclay particles on non-isothermal crystallisation and degradation behaviour of PP/LDPE blend composites, Polymers (Basel). 10 (3) (2018).
[48] B. Chen, S. Berretta, K. Evans, K. Smith, O. Ghita, A primary study into graphene/polyether ether ketone (PEEK) nanocomposite for laser sintering, Appl. Surf. Sci. 428 (2018) 1018–1028.
[49] A. Almansoori, et al., Surface modification of the laser sintering standard powder polyamide 12 by plasma treatments, Plasma Process. Polym. 15 (7) July) (2018) 1800032.
[50] S.G. Lei, S.V. Hoa, M.T. Ton-That, Effect of clay types on the processing and properties of polypropylene nanocomposites, Compos. Sci. Technol. 66 (10) (2006) 1274–1279.
[51] C.Z. Yan, Y.S. Shi, J.S. Yang, J.H. Liu, An organically modified montmorillonite/nylon-12 composite powder for selective laser sintering, Rapid Prototyp. J. 17 (1) (2011) 28–36.
[52] K. Masenelli-Varlot, E. Reynaud, G. Vigier, J. Varlet, Mechanical properties of clay-reinforced polyamide, J. Polym. Sci. Part B: Polym. Phys. 40 (3) (2002) 272–283.